Fifth International Symposium on Marine Propulsion
smp'17, Espoo, Finland, June 2017

Unsteady Hydrodynamic Modeling of a Cycloidal Propeller

Atanu Halder
halder.atanu360@gmail.com
Graduate Research Assistant

Carolyn Walther
carolyn.walther@tamu.edu
Graduate Research Assistant

Moble Benedict
moblebenedict@gmail.com
Assistant Professor

Department of Aerospace Engineering
Texas A&M University, College Station, TX 77843, USA

ABSTRACT

In this paper, a lower-order unsteady hydrodynamic model of a cycloidal propeller along with in-house experiments to validate the model is presented. Towards this, the hydrodynamics of a cycloidal propeller is investigated thoroughly and various underlying physical phenomena such as dynamic virtual camber, effects of near and shed wake, leading edge vortices are rigorously modeled. It is shown that the chord-wise variation of incidence velocity angle on cycloidal propeller blade is manifested as dynamic virtual camber, which depends on curvilinear flow geometry, pitch angle, pitch rate and also inflow distribution. By including all these effects together, a generalized expression of additional lift due to virtual camber effect is developed. To capture the effects of near wake, a nonlinear lifting line model is incorporated. Rapid pitching of rotor blades produces unsteady phenomena such as strong leading edge vortices and shed wakes. Polhamus leading edge suction analogy is applied to model leading edge vortex. To capture effects of shed wake, a method based on Theodorsen's approach has been developed. A modified Double Multiple Streamtube (D-MS) model is used for modeling the complex inflow characteristics of a cycloidal propeller. The present hydrodynamic model is validated with measured time-history of forces obtained from in-house experiments at low Reynolds numbers.

Keywords

UUV (Unmanned Underwater Vehicle), Cycloidal Propeller, Dynamic Virtual Camber, Inflow, Wake

NOTATION

c	Chord Length
C_d	Drag coefficient
$C_{d_{le}}$	Drag coefficient with leading edge vortex
$C_{d_{wole}}$	Drag coefficient without leading edge vortex
C_l	Lift coefficient
$C_{l_{le}}$	Lift coefficient with leading edge vortex
$C_{l_{quasy\_steady}}$	Quasi-steady lift coefficient
$C_{l_{unsteady}}$	Unsteady lift coefficient
$C_{l_{wole}}$	Lift coefficient without leading edge vortex
D	Drag
F_u	Force on the blade along the direction of flow at upstream
F_d	Force on the blade along the direction of flow at downstream
f_u	Force per unit area along the direction of flow at upstream
f_d	Force per unit area along the direction of flow at downstream
k_f	Reduced frequency
K_v	Non-dimensional coefficient due to extra vortex lift by leading edge suction
L	Lift
$\dot{m}$	Mass flow rate
N_b	Number of blades in cycloidal propeller
R	Radius of cycloidal propeller
$R'(x)$	Distance of local blade location (x) from center of cycloidal propeller
U_T	Component of resultant flow velocity along the direction of blade
U_P	Component of resultant flow velocity along the perpendicular direction of blade
$\vec{V}_b(x)$	Blade velocity at a particular chord-wise location(x) on propeller blade
V_d	Downstream inflow velocity
V_{d_wake}	Downstream wake velocity
$\vec{V}_i(x)$	Inflow velocity at a particular chord-wise location (x) on propeller blade
$\vec{V}_p(x)$	Relative flow velocity at a particular chord-wise location (x) on propeller blade due to blade pitching
$\vec{V}(x)$	Resultant flow velocity at a particular chord-wise location (x) on propeller blade
V_u	Upstream inflow velocity
V_{u_wake}	Upstream wake velocity

V_∞	Free stream velocity
α_{eff}	Effective angle of attack
α_i	Induced angle of attack
α_x	Angle of attack at a particular chord-wise location (x) on propeller blade
β	Angle between inflow velocity and vertical axis
Γ	Circulation
γ_d	Inflow angle at downstream locations
γ_u	Inflow angle at upstream locations
θ	Prescribed blade pitch
ρ	Fluid density
σ	Solidity
Ψ	Azimuthal location of blade in a cycle
Ω	Rotational speed of rotor

1 INTRODUCTION

In past few decades, unmanned underwater vehicles (UUVs) have become popular among researchers and scientists due to its wide range of applications and future possibilities. UUVs have huge potential for oceanographic studies such as deep water and shallow water marine exploration, as well as military applications such as maritime intelligence/surveillance/reconnaissance (ISR), mine countermeasures, anti-submarine warfare, inspection/identification, communication, payload delivery, information operations and time critical strike (U.S. Navy 2004). Oil and gas industry is also becoming interested in application of UUVs for pipeline inspection and surveillance, sea-floor mapping etc. Most of the common UUVs use conventional screw propellers which are mechanically simple and moderately efficient in steady cruise (Blidberg 2001, Griffiths et al 2004, Collar et al 1994, Bandyopadhyay 2009). However, a UUV using a single fixed conventional propeller would suffer from low agility and would be highly susceptible to disturbances, especially during station-keeping. To overcome this barrier many UUVs are designed with multiple propellers in staggered arrangements to generate thrust in different directions to improve control authority. Although these types of configurations can offer superior maneuverability, many of these additional propellers/motors become redundant in forward motion, which adds to the weight and reduces efficiency (Roper et al 2011). Thrust production on conventional propellers relies on steady hydrodynamic mechanisms and it is challenging to keep a steady flow attached to the hydrofoil surface, especially at low Reynolds numbers. Therefore, a conventional propeller blade can only operate over a narrow range of angle of angle of attack, if the flow has to stay attached. This leads to small stall margins and the slightest perturbation could cause the flow to separate. On the other hand, in nature, fish fins and tail operate in a highly unsteady hydrodynamic regime with large variations in angle of attack and are more robust to perturbations. For this reason, bio-inspired and biomimetic propulsion systems, that exploits unsteady hydrodynamics just like natural swimmers, have been investigated for the last two decades, dating back to the RoboTuna developed at MIT during the mid-90s (Anderson 1996, Read 1999, Haugsdal 2000, Flores 2003, Polidoro 2003). Although many of these bio-inspired robotic UUVs could be more efficient, they used complex linkage systems powered with multiple servo motors or hydraulic/pneumatic actuators, which resulted in enormous mechanical complexity and weight when compared to conventional propellers (Kato 1998, Triantafyllou 2004, Phillips et al 2010, Zhou & Low 2012, Palmre et al 2013). Some recent studies investigated the use of smart materials such as shape memory alloys to actuate the motion, introducing other limitations such as bandwidth (Low 2011, Roper et al 2011). In the present study, a cycloidal propulsion system based UUV (Fig. 1) is proposed. Cycloidal propellers exploit unsteady hydrodynamics for efficient thrust production while it also offers high maneuverability through instantaneous thrust vectoring.

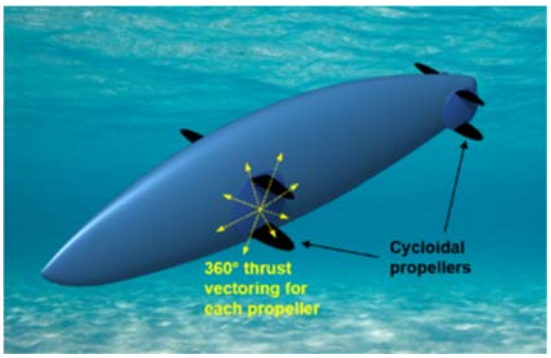

Fig. 1: Cycloidal propeller based unmanned underwater vehicle (UUV).

As shown in Fig. 1, in the case of a cycloidal propeller, the blade span is parallel to the axis of rotation of the propeller. As shown in Fig. 2, the pitch angle of each blade is cyclically altered in such way that the blade experiences positive geometric angles of attack at both the top (upstream) and bottom (downstream) halves of the azimuth cycle resulting in a net thrust. Magnitude of net thrust can be changed by varying amplitude of blade pitch or by varying rotational speed; while direction of the net thrust vector can be altered by varying phase of cyclic blade pitch. The main advantage of the cycloidal propulsion system is that a complete 360^0 instantaneous thrust vectoring can be achieved by simply phase-shifting the cyclic pitch which could potentially improve the agility and disturbance rejection capability of a UUV propelled using this concept. This could also be more power efficient and significantly faster than swiveling a conventional screw-propeller. There have been many recent studies (Jarugumilli et al 2013a, Jarugumilli et al 2013b, Benedict et al 2013a, Benedict et al 2013c, Benedict et al 2014a, Benedict et al 2014b, Zachary et al 2013, Shrestha et al 2012, Shrestha et al 2014, Hrishikeshavan et al 2014) on cycloidal rotor systems for small-scale aerial vehicle applications, which showed that an optimized cycloidal rotor can be more efficient than conventional rotors (Benedict 2010, Benedict et al 2011a,

Benedict et al 2013b). The fundamental reason behind this is decrease in induced power requirement due to uniform load distribution along blade span which also reduces rotor speed required to generate a certain thrust. Also, unsteady fluid dynamic mechanisms such as leading edge vortices improve performance of cycloidal propulsion system, as revealed by Particle Image Velocimetry (PIV) studies (Benedict et al 2010a, Benedict et al 2010b). Furthermore, due to dynamic pitching at high amplitudes and reduced frequencies, cycloidal propeller blades can potentially exploit dynamic stall to generate very high lift coefficients, even twice the static values (Walther et al 2017).

For underwater applications, cycloidal propellers (commonly called Voith Schneider Propellers or VSPs) have been historically used on tug-boats, mine-sweepers and other applications which require high thrust at low speeds, which could be easily vectored for tight maneuvering, station-keeping, etc (Haberman & Harley 1961, Haberman & Caster 1962, Sparenberg & De Graaf 1969, Ficken & Dickerson 1969, James 1971, Zhu 1981). Notably, there have been only a limited number of studies on cycloidal propellers for marine applications, especially at high advance ratios (Dickerson & Dobay 1970, Bose & Lai 1989). A detailed literature survey on the research on cycloidal marine propellers is provided in Bartels (2006).

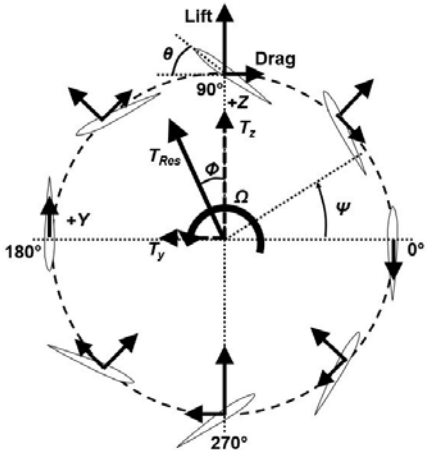

Fig. 2: Cycloidal propeller blade kinematics.

Fig. 3: Voith-Schneider propellers installed under the ship hull.

It is significant to note that, not many systematic scientific studies have been conducted to unravel the complex unsteady fluid dynamics of cycloidal propellers in order to fully exploit its potential. In the present literature, there are very limited experimental data as well as analytical models that can predict performance of a cycloidal propeller, especially, for underwater propulsion. Moreover, all the previous analytical models were only validated with time-averaged performance measurements. First attempt to develop an aerodynamic model for cycloidal rotor was carried out by Wheatley in 1930s (Wheatley 1933, Wheatley & Windler 1935). The model predictions were compared with time-averaged wind-tunnel measurements; however, it showed poor correlation with experimental data. Recently, more fluid-dynamic models were developed by McNabb (2001), Kim et al. (2004) and Hwang et al (2005, 2006). However, these studies were performed on large scale cycloidal rotors operating at higher Reynolds numbers and showed good correlation with time-averaged thrust and power measurements. At MAV scales, CFD studies were carried out by Iosilevskii and Levy (2006), which showed good correlation with experimental results and also exposed some of the complex underlying fluid dynamic phenomena. Recently an aeroelastic model of cycloidal rotor was developed by Benedict et al (2011b), which utilized a simplified aerodynamic model and mainly focused on understanding effects of flexible blade deflections on cycloidal rotor performance. Recently Voith Schneider propellers (VSP) have attracted significant attention from researchers. In Esmailian et al (2014), CFD simulations have been carried out to predict VSP performance . Some studies have been carried out to develop simplified models of VSP (Jürgens et al 2007).

However, there have been very limited efforts to develop a lower order high fidelity hydrodynamic model that could be utilized for design and optimization of cycloidal propeller. Existing models lack detailed modeling of the physics of cycloidal propellers and therefore, these models are not capable of accurately predicting instantaneous blade fluid-dynamic forces. None of the previous studies on cycloidal propellers provide information on the unsteady flow phenomena including dynamic virtual camber/incidence and dynamic stall on the blades. Therefore, the present paper focuses on the development of a detailed high-fidelity unsteady hydrodynamic model, which is capable of predicting not only the time averaged forces, but also the time history of forces on a cycloidal propeller blade. At the same time, the present model is computationally inexpensive that it can be used for design optimization of cycloidal propellers. To achieve this goal, key fluid-dynamic phenomena on a cycloidal propeller are investigated and rigorous modeling of virtual camber, effects of near and shed wakes, leading edge vortices are carried out. Moreover, the inflow model is improved by modifying existing Double Multiple Streamtube (D-MS) model. All these improvements enabled the model predictions to

correlate extremely well with the time-history of forces obtained from in-house experimental data. The long term goal of this project is to develop a high-fidelity hydroelastic cycloidal propeller model to be used in a computational design framework for next generation of cycloidal propeller based UUVs.

2 METHODOLOGY

Large amplitude, high reduced frequency pitching motion of cycloidal propeller blades results in highly complex unsteady hydrodynamics characterized by strong leading edge vortex formation, nonlinear dynamic virtual camber effects, shed wake and blade-wake interactions. For accurate prediction of this complex physical system, detailed CFD modeling is necessary which is out of scope for the present application, where the objective is to develop a design code for a cycloidal propeller. Therefore, a high fidelity lower-order model has been developed which can predict instantaneous blade hydrodynamic forces and propeller performance (cycle-averaged thrust and power) with sufficient accuracy. The first step in the proposed hydrodynamic model is to compute the magnitude and incident angle of the resultant flow velocity at each local chord-wise location of propeller blade. For this purpose, blade speed is obtained from prescribed kinematics and flow speed is obtained from inflow information. Chord-wise variation of incident flow angle is manifested as virtual camber effect which is discussed in detail in the subsequent sections. Once sectional angle of attack is obtained, sectional quasi-steady fluid-dynamic forces are computed using thin-airfoil theory. In the next step, several models are developed to incorporate effects of near and shed wakes and leading edge vortices. Using these models, unsteady fluid-dynamic forces on propeller blades are obtained. An iterative procedure is used to calculate inflow and circulation, which are computed from the obtained blade forces and iterated until both circulation and inflows are converged.

2.1 Dynamic Virtual Camber

The cycloidal propeller blades experience a unique phenomenon known as virtual camber. The virtual camber effect occurs due to the chord-wise variation of the incident velocity angle (or angle of attack) on the hydrofoil. This effect is very predominant in cycloidal propellers because the flow over a cycloidal propeller blade is characterized by a pitching hydrofoil in a curvilinear flow in the presence of inflow that varies along with azimuth. A hydrofoil in a curvilinear flow experiences different flow velocity magnitude and direction along the chord due to geometry and the curvilinear nature of the flow; this manifests as an effective camber and incidence. Figure 4 shows how curvilinear flow geometry creates a negative virtual camber effect for a blade at 0° pitch angle. Therefore, a symmetric blade immersed in a curvilinear flow will behave like a cambered blade in a rectilinear flow as shown in Fig. 4. This phenomenon is more significant for cycloidal propellers with a large chord-to-radius ratio (c/R).

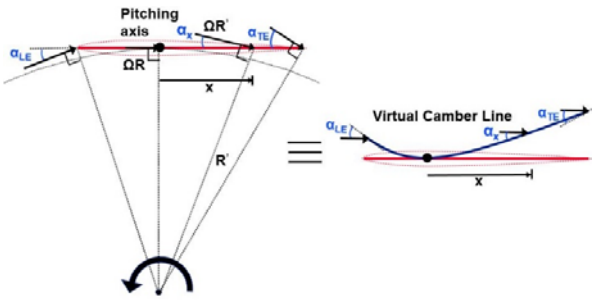

Fig. 4: Negative virtual camber effect due to curvilinear flow.

Flow over a cycloidal propeller is not purely curvilinear when it is producing thrust because of the induced flow velocity, which also effects virtual camber and incidence (Fig. 5).

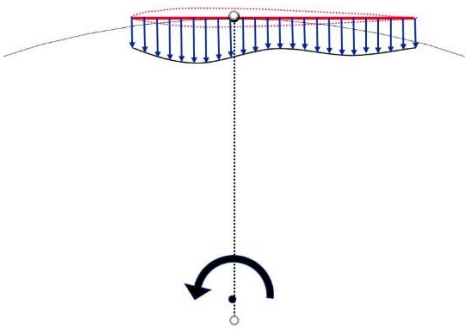

Fig. 5: Chord-wise variation of flow velocity due to inflow distribution.

Additionally, the blade pitch angle and pitch rate also affects the chord-wise velocity distribution and therefore, virtual camber. Figure 6 shows pitch rate causing chord-wise variation of flow incidence angle which is manifested as a positive virtual camber effect. An opposite pitch rate (nose-down pitch) would cause a negative virtual camber effect.

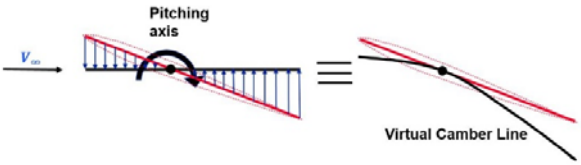

Fig. 6: Positive virtual camber effect due to pitch rate.

Since blade pitch and pitch rate vary with azimuthal location, corresponding virtual camber also changes with azimuth making it dynamic virtual camber. To consider all these effects together, a generalized expression has been derived to represent the variation of local angle of attack (α_x) along blade chord.

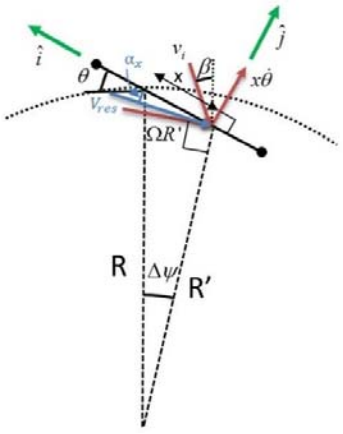

Fig. 7: Velocity components at a local chord location on cycloidal propeller blade.

All the velocity components of fluid relative to propeller blade is shown at Fig. 7. All the velocity components are computed along tangential ($\hat{\imath}$) and normal ($\hat{\jmath}$) to propeller hydrofoil chord. Blade velocity obtained from kinematics of propeller can be expressed as Eq. 1.

$$\vec{V}_b(x) = \Omega R'\cos(\theta - \Delta\psi)\hat{i} - \Omega R'\sin(\theta - \Delta\psi)\hat{j} \quad (1)$$

Using geometrical relations, blade velocity can be rewritten as Eq. 2.

$$\vec{V}_b(x) = \Omega R\cos\theta\hat{i} - \Omega(R\sin\theta - x)\hat{j} \quad (2)$$

Flow velocity relative to propeller blade due to blade pitching is given as

$$\vec{V}_p(x) = x\dot{\theta}\hat{j} \quad (3)$$

The inflow speed is represented as $v_i(x)$ acting on propeller blade at an angle $\beta(x)$ w.r.t vertical axis. Thus, inflow velocity can be expressed as

$$\vec{V}_i(x) = -\left(v_i\sin(\beta+\theta)\hat{i} + v_i\cos(\beta+\theta)\hat{j}\right) \quad (4)$$

Considering all the above effects, the net relative flow velocity with respect to propeller blade is calculated (Eq. 5).

$$\vec{V}(x) = \vec{V}_p(x) + \vec{V}_i(x) - \vec{V}_b(x) \quad (5)$$

Substituting, Eq. 2, 3 and 4 into Eq. 5, the net flow velocity can be expressed as

$$\vec{V}(x) = -U_T\hat{i} - U_P\hat{j} \quad (6)$$

Where,

$$U_T = \Omega R\cos\theta + v_i\sin(\beta+\theta) \quad (7)$$

$$U_P = x(\Omega - \dot{\theta}) + v_i\cos(\beta+\theta) - \Omega R\sin\theta \quad (8)$$

This information all together gives net flow speed ($V(x)$) and incident angle of attack ($\alpha_x(x)$) at each local chord-wise location (Eq. 9 and 10)

$$V(x) = \sqrt{U_T^2 + U_P^2} \quad (9)$$

$$\alpha_x(x) = -\tan^{-1}\left(\frac{x(\Omega-\dot{\theta}) + v_i\cos(\beta-\theta) - \Omega R\sin\theta}{\Omega R\cos\theta + v_i\sin(\beta+\theta)}\right) \quad (10)$$

In the above expression, v_i is assumed to be zero for first iteration and updated using inflow model (modified D-MS model, discussed later) for subsequent iterations. In Eq. 10, θ is geometric pitch angle of cycloidal propeller blade. For a cambered airfoil in straight flow, the local angle of attack varies along chord according to following equation (Eq. 11).

$$\alpha_x(x) = \theta - \frac{dy}{dx}(x) \quad (11)$$

By comparing, Eq. 10 and Eq. 11, expression for virtual camber line of cycloidal propeller blade is obtained (Eq. 12).

$$\frac{dy}{dx} = \theta + \tan^{-1}\left(\frac{x(\Omega-\dot{\theta}) + v_i\cos(\beta-\theta) - \Omega R\sin\theta}{\Omega R\cos\theta + v_i\sin(\beta+\theta)}\right) \quad (12)$$

Modified thin airfoil theory has been used to calculate steady lift from the chord-wise variation of incidence. For this purpose, airfoil co-ordinates are transformed along chord line. Figure 8 shows co-ordinate transformation from actual chord-line (x, y) to virtual chord-line (X, Y) and Equations 13 and 14 provide expressions for this co-ordinate transformation.

$$X = (y - y_1)\sin\phi + (x - x_1)\cos\phi \quad (13)$$

$$Y = (y - y_1)\cos\phi - (x - x_1)\sin\phi \quad (14)$$

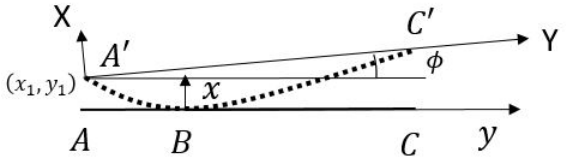

Fig. 8: Co-ordinate transformation from physical airfoil co-ordinate to virtual cambered airfoil co-ordinate.

Since, the rotor blades in a cycloidal propeller goes through high angles of attack, small angle of attack assumption is relaxed while using thin airfoil theory and a more general expression (Eq. 15) is used.

$$C_l = C_{l_\alpha}\sin\alpha + C_{l_0} \quad (15)$$

In the above equation, C_{l_o} is additional lift due to the effects of virtual camber. C_{l_o} is a complex function of incidence angle given by Eq. 16. In this equation, $\frac{dY}{dX}$ is obtained from Eq. 10, 13 and 14. $\frac{dY}{dX}$ represents slope of virtual camber line in transformed co-ordinate X-Y. Using numerical integration procedure, C_{l_o} is computed. In Eq. 16, non-dimensional parameter η is used ($x = \frac{c}{2}(1 - \cos\eta)$) for integration purposes.

$$C_{l_0} = 2\cos\alpha\int_0^{\pi}\frac{dY}{dX}(\cos\eta - 1)\,d\eta \quad (16)$$

2.2 Nonlinear Lifting Line Model

A nonlinear lifting line theory is implemented numerically to incorporate the effects of near wake and tip vortices (finite-span effect). For this purpose, the wing is divided into number of span-wise elements. Nodal point is set to center of each element. Induced angle of attack at each nodal point is obtained using following formula (Eq. 17).

$$\alpha_i(y_0) = \frac{1}{4\pi V_\infty} \int_{-b/2}^{b/2} \frac{d\Gamma / dy}{y_0 - y} dy \qquad (17)$$

Above integral is computed numerically using Gauss-quadrature integration rule (11 gauss quadrature points are used for this purpose). From this, effective angle of attack at each nodal point is obtained using $\alpha_{eff}(y_0) = \alpha(y_0) - \alpha_i(y_0)$. Effective angle of attack is used to calculate quasi-steady lift using Eq. 15. Circulation is computed at the center of each element from calculated lift $L = \rho V_\infty \Gamma$. For the first iteration, suitable values of circulation (based on elliptical lift distribution) are assumed and circulation is updated from lift calculated at each iteration until convergence is obtained. At each iteration, circulation is updated using $\Gamma_{new} = \Gamma_{old} + D(\Gamma_{new} - \Gamma_{old})$, where D is an update parameter and suitably chosen for proper convergence (0.05 in present simulations).

2.3 Unsteady Effects

Rapid pitching of rotor blade produces strong unsteady phenomena such as leading edge vortex and shade wake. To capture effect of shed wake, an unsteady model based on Theodorsen's approach has been developed. Theodorsen's function has been originally developed to calculate circulatory lift produced by sinusoidal variation of angle of attack and pitch angle. Due to inclusion of virtual camber and its nonlinear behavior, the oscillatory part of the lift of a cycloidal propeller blade contains not just the first harmonic, rather it shows high frequency components with varying phase delays. To handle this, an automated function has been developed that would perform Fourier series decomposition of oscillatory part of lift (due to shed wake) and compute corresponding frequency and Theodorsen's function to generate unsteady lift. Fourier decomposition of quasi-steady lift coefficient can be expressed as following (Eq. 18).

$$C_{l_{quasi\_steady}} = a_0/2 + \sum_{i=1}^{n} a_n \cos i\Omega t + b_n \sin i\Omega t \qquad (18)$$

First harmonic of quasi-steady lift coefficient Cl_{quasi_steady} is Ω and corresponding reduced frequency is $k_f = \Omega c/2V$. Theodorsen's function corresponding to higher harmonics are computed to calculate unsteady lift coefficient (Eq. 19).

$$C_{l_{unsteady}} = a_0/2 + \sum_{i=1}^{n} \left(a_n \cos i\Omega t + b_n \sin i\Omega t\right) C\left(ik_f\right) \qquad (19)$$

In the above equation, $C(ik_f) = F(ik_f) + jG(ik_f)$ is Theodorsen's function corresponding to reduced frequency $k_i = ik_f$, where i varies from 1 to n.

2.4 Leading Edge Vortex

High amplitude pitching of rotor blade creates strong leading edge vortex on cycloidal propeller, as shown by some of the on-going in-house experimental studies (Walther et al 2017). Figure 9 shows PIV measured flowfield showing large leading edge vortex formation. Leading edge vortex delays flow separation on rotor blade which significantly improves lift performance of rotor at high pitch angles enabling rotor to operate even at $\pm 45^0$ pitch amplitudes. Polhamus leading edge suction analogy (Polhamus 1966 & 1968) is applied to model leading edge vortex. Additional lift (vortex lift) due to leading edge vortex and additional drag due to leading edge separation are modeled using this suction analogy.

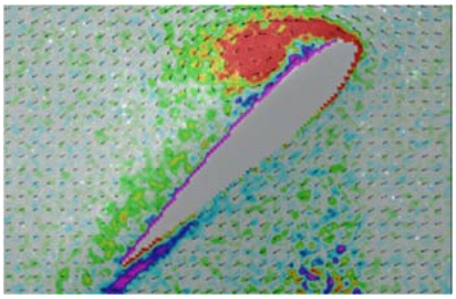

Fig. 9: Formation of large leading edge vortex from PIV measurements at pitch amplitude = $\pm 45^0$ and 90^0 azimuth.

$$C_{l_{le}} = C_{l_{wole}}\left(\cos^2\alpha + \eta \sin^2\alpha\right) + K_v \cos\alpha \sin^2\alpha \qquad (20)$$

$$C_{d_{le}} = C_{l_{wole}} \sin\alpha \cos\alpha (1-\eta) + K_v \sin^3\alpha \qquad (21)$$

In the above equation, Cl_{le}, Cd_{le} are lift and drag coefficient with leading edge suction and Cl_{wole}, Cd_{wole} are lift and drag coefficient without leading edge suction. K_v is non-dimensional coefficient related to additional vortex lift generated by leading edge vortex. η represents percentage of leading edge suction. $\eta = 1$ means no leading edge suction and $\eta = 0$ means complete leading edge suction.

2.5 Force Computation

Once lift and drag coefficients, C_l and C_d, are computed, lift and drag force in blade co-ordinate system is obtained using lift, $L = \frac{1}{2}\rho V^2 S C_l$ and drag, $D = \frac{1}{2}\rho V^2 S C_d$. Forces in blade co-ordinate are transformed into inertial co-ordinate using proper transformation matrices. To calculate time-averaged propeller thrust, blade force is multiplied with solidity, $\sigma = N_b c/(2\pi R)$ and averaged over one revolution.

2.6 Inflow Model

Previously in the analysis of cycloidal rotors and vertical axis wind turbines, Single Streamtube inflow or Double Multiple Streamtube (D-MS) models have been mostly used (Benedict et al 2011b). For Single Streamtube model, the inflow is considered uniform along the azimuth and inflow at top and bottom halves of the blade is assumed to be same. Therefore, no blade interaction or wake effect is considered after the flow passes through the upper-half. This assumption is not physical. On the

other hand, for D-MS model, there is azimuthal variation in inflow magnitude, however, inflow direction is assumed to be radial to blade path in the upper half in the hover state, which is also not physically realistic.

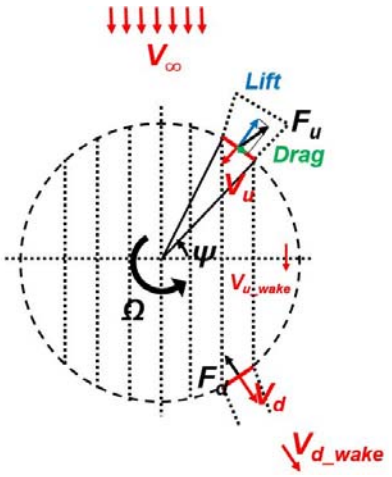

Fig. 10 Schematic of inflow model.

In the present hydrodynamic model (schematic shown in Fig. 10), the proposed inflow model (modified D-MS model) relaxes these assumptions. In this model, it is assumed that various streamlines (denoted by s) interacts with the rotor blade twice, upstream and downstream, with different inflow velocity magnitude and direction. Two adjacent streamlines form a streamtube. Unlike D-MS model, this modified model calculates the inflow direction based on resultant force direction on the blade at that particular azimuthal location (Eq. 22). The underlying reasoning behind this approach is that at a local azimuthal location, whatever hydrodynamic force the propeller blade experiences, it exerts same force to the nearby fluid in the opposite direction. When the rotor blade starts rotating, it would accelerate nearby fluid opposite to the direction of resultant force blade is experiencing (Fig. 11).

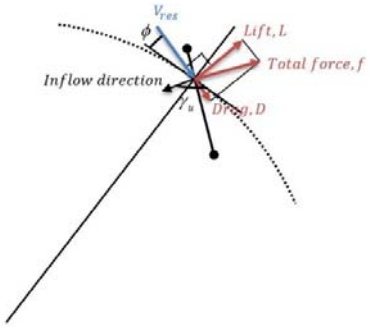

Fig. 11 Schematic of inflow model.

$$\gamma_u = \pi - \phi - \tan^{-1}\left(\frac{D}{L}\right) \tag{22}$$

In Eq. 22, γ_u is inflow angle at upstream locations, ϕ is the angle between local tangent and resultant flow velocity with respect to propeller blade (Fig. 11). Once the inflow direction is calculated based on above approach, actuator surface theory and mass and momentum conservation laws were applied to determine magnitude of inflow velocity (Eq. 14, 16) at upstream (V_u) and downstream (V_d). The wake velocity of completely expanded flow after interacting with upstream blade is denoted as V_{u_wake} and wake velocity after interacting with downstream blade is denoted as V_{d_wake} . Using actuator surface theory, inflow velocities can be expressed as Eq. 23 and Eq. 24.

$$V_u(s) = \frac{1}{2}\left(V_\infty + V_{u\_wake}(s)\right) \tag{23}$$

$$V_d(s) = \frac{1}{2}\left(V_w(s) + V_{u\_wake}(s)\right) \tag{24}$$

Force exerted by fluid on the propeller blade on upstream (F_u) and downstream (F_d) can be expressed as Eq. 25 and Eq. 26, respectively.

$$F_u(s) = \dot{m}\left(V_\infty - V_{u\_wake}(s)\right) \tag{25}$$

$$F_d(s) = \dot{m}\left(V_{u\_wake}(s) - V_w(s)\right) \tag{26}$$

Where, $\dot{m}$ is the mass flow rate. Using continuity theory, above equations can be rewritten as Eq. 27 and Eq. 28.

$$F_u = \rho V_u A \sin\gamma_u (V_\infty - V_{u\_wake}) \tag{27}$$

$$F_d = \rho V_d A \sin\gamma_d (V_{u\_wake} - V_w) \tag{28}$$

By comparing Eq. 23 and Eq. 27, upstream inflow velocity (V_u) and upstream wake velocity (V_{u_wake}) can be obtained (Eq. 29 and Eq. 30).

$$V_u(s) = \frac{V_\infty}{2} + \sqrt{\frac{V_\infty^2}{4} - \frac{f_u(s)}{2\rho\sin\gamma_u(s)}} \tag{29}$$

$$V_{u\_wake}(s) = V_\infty - \frac{f_u(s)}{\rho V_u(s)\sin\gamma_u(s)} \tag{30}$$

In the above equations, f is force per unit area along the direction of flow. In the similar procedure, downstream inflow velocity (V_d) and downstream wake velocity (V_{d_wake}) can be obtained (Eq. 31 and Eq. 32) by comparing Eq. 24 and Eq. 28.

$$V_d(s) = \frac{V_{u\_wake}(s)}{2} + \sqrt{\frac{V_{u\_wake}(s)^2}{4} - \frac{f_u(s)}{2\rho\sin\gamma_u(s)}} \tag{31}$$

$$V_{d\_wake}(s) = V_{u\_wake}(s) - \frac{f_d(s)}{\rho V_d(s)\sin\gamma_d(s)} \tag{32}$$

Once. the inflow is updated using above Equations (29-32), hydrodynamic forces are calculated based on new inflow and circulation. These steps are repeated until both circulation and inflow are converged.

3 MODEL VALIDATION

Due to the dearth of experimental data in the present literature on time-history of hydrodynamic forces on cycloidal propeller blade, in-house experiments were carried out and the present hydrodynamic model is validated with the results obtained from these experiments.

3.1 Experimental Setup

For model validation, a test setup (Fig. 12) is developed where a single bladed cycloidal propeller is tested inside a water tank at a Reynolds number of around 18,000. Forces and moments are measured using a miniature 6-component force balance at the blade root. A 12-channel slip ring is used to transfer the signals from the force balance in the rotating frame to the data acquisition equipment in the stationary frame. The blade pitching is controlled using an analog servo, which allows us to prescribe specific pitching kinematics for a test. The experiments are first conducted in air which provide the inertial forces; then the same experiments are repeated in water. The pure hydrodynamic forces are obtained by subtracting the inertial forces from the force measurements made in water.

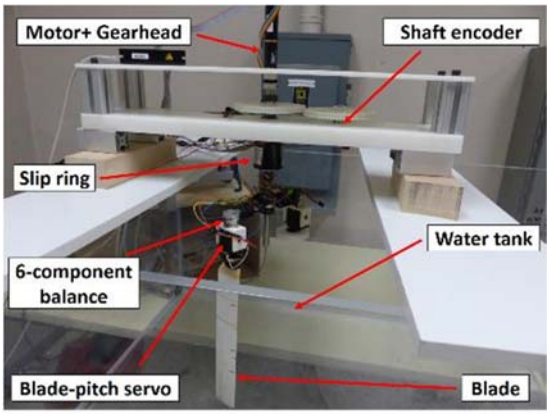

Fig. 12 Single-bladed cycloidal propeller test rig in water tank.

3.2 Results

Dynamic pitching experiments are conducted with a single bladed cycloidal propeller at 40 rpm. Propeller blade has chord of 2 inches and span of 12 inches and pitched at quarter chord location. Radius of cycloidal propeller is 3.43 inches. Figures 13 and 14, respectively, show the comparison between measured forces and predictions from the present hydrodynamic model. The figures show the variation of radial and tangential force coefficients as a function of blade azimuthal location over a range of pitch amplitudes (±20° to ±45°). The results show good correlation between the present hydrodynamic model prediction and test data. It is also interesting to see both from the experiment and analysis that the blades are producing higher radial and tangential forces at the lower half (ψ = 180° – 360°) than the upper half (ψ = 0° – 180°). The reason for this will be explained in the discussion section.

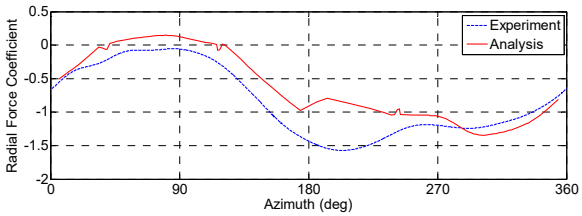

Fig. 13a Pitch Amplitude 20^0.

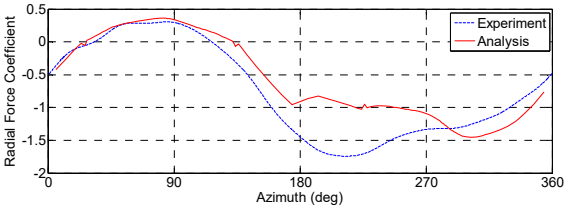

Fig. 13b Pitch Amplitude 25^0.

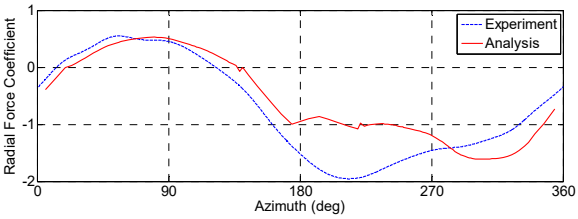

Fig. 13c Pitch Amplitude 30^0.

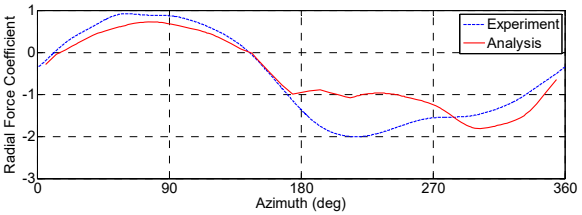

Fig. 13d Pitch Amplitude 35^0.

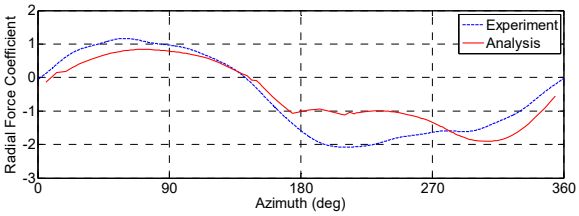

Fig. 13e Pitch Amplitude 40^0.

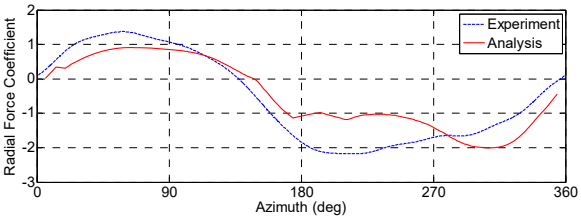

Fig. 13f Pitch Amplitude 45^0.

Fig. 13 Radial force coefficient as a function of azimuth (Experiment vs. Analysis).

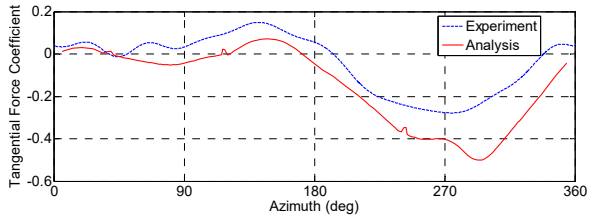

Fig. 14a Pitch Amplitude 20^0.

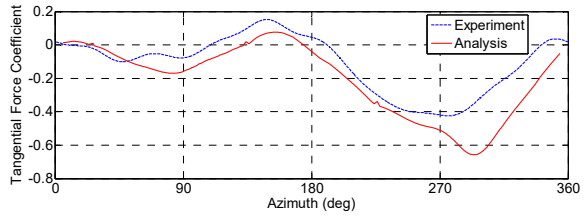

Fig. 14b Pitch Amplitude 25^0.

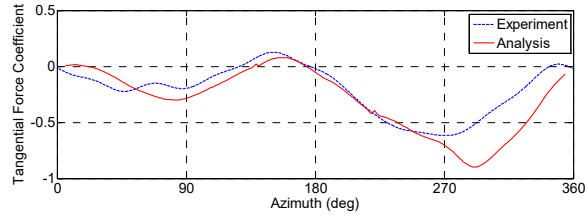

Fig. 14c Pitch Amplitude 30^0.

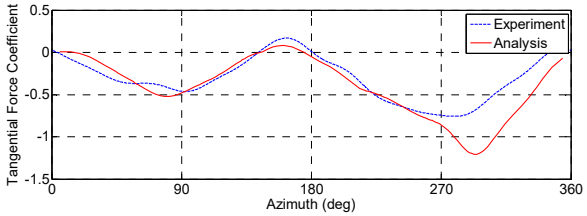

Fig. 14d Pitch Amplitude 35^0.

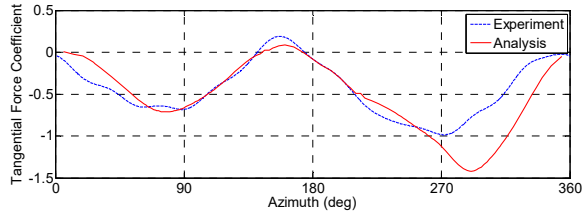

Fig. 14e Pitch Amplitude 40^0.

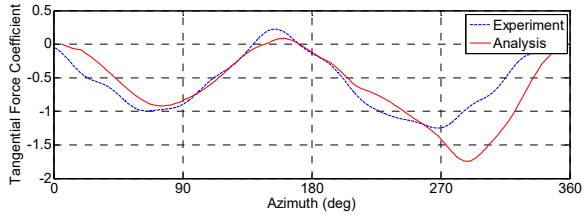

Fig. 14f Pitch Amplitude 45^0.

Fig. 14 Tangential force coefficient as a function of azimuth (Experiment vs. Analysis).

4 DISCUSSION

Once the hydrodynamic model is validated with in-house experimental data, it is used to investigate physics behind thrust production of a cycloidal propeller. In the following subsections details of various phenomena are discussed in depth.

4.1 Cause and Effect of Dynamic Virtual Camber

As shown by Eq. 16, virtual camber manifests as additional lift on the blade. Figure 15a shows variation of additional lift coefficient (C_{l_o}) due to virtual camber along azimuthal location for a cycloidal propeller blade rotating at 40 rpm with 35^0 pitch amplitude and figures 15b and 15c show corresponding prescribed pitch and pitch rate (measured values), respectively, as blade goes through various azimuthal locations. It shows effects of curvilinear flow, pitch, pitch-rate and inflow on virtual camber and therefore, on additional lift. From Fig. 15a it can be observed that virtual camber effect due to only curvilinear geometry (magenta line) is static in nature and it always causes negative virtual camber leading to negative C_{l_o}. While pitch, pitch rate and inflow creates time-dependency of virtual camber effect making it a *dynamic* virtual camber. Figure 15a reveals that pitch and especially pitch rate creates a very dominant and characteristic virtual camber effect unlike inflow distribution which is more random in nature.

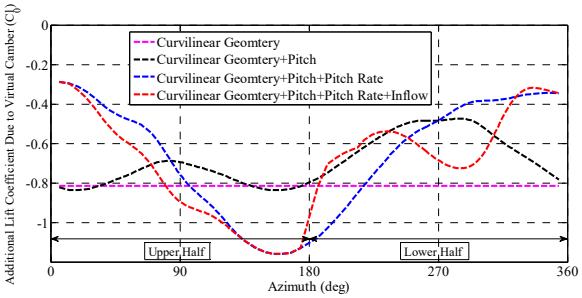

Fig. 15a Variation of additional lift coefficient due to virtual camber.

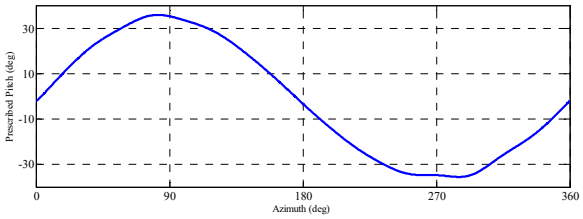

Fig. 15b Measure blade pitch along azimuth.

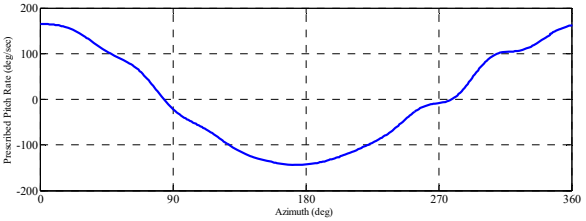

Fig. 15c Measured pitch rate along azimuth.

Fig. 15 Effect of Virtual Camber due to various phenomena.

Figure 15a shows that blade pitch decreases negative virtual camber and opposes the effects of curvilinear geometry. The effect of blade pitch is more prominent near 90^0 and 270^0 azimuth since pitch angle reaches at its peak at those locations (Fig. 15b). It is also observed that pitch rate creates positive virtual camber effect near 0^0 azimuth, which almost nullifies the effects of curvilinear geometry; while at 180^0, it creates negative virtual camber which together with curvilinear effect produces even larger negative lift. For this reason, as seen from Fig. 13, the net radial force coefficient is near zero at 0^0 azimuth, while it is much below zero at 180^0 azimuth, although pitch angle is near 0^0 at both azimuth locations (Fig. 15b). Pitch rate effect on virtual camber is dominant at 0^0 and 180^0 azimuth because pitch rate reaches its peak near these two locations (Fig. 15c). Figure 16 shows graphically how pitch rate is creating opposite virtual camber effects at different azimuth locations.

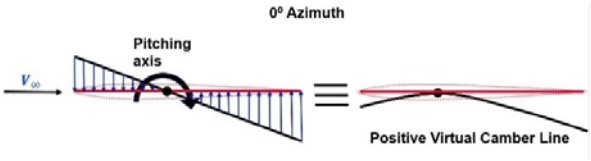

Fig. 16a Pitch rate effect at 0^0 azimuth

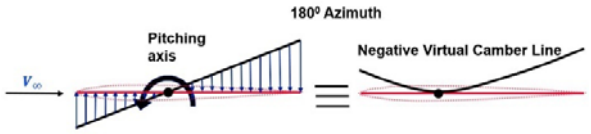

Fig. 16b Pitch rate effect at 180^0 azimuth

Fig. 16 Effect of Pitch rate on dynamic virtual camber at two extreme azimuthal locations (0^0 and 180^0).

This phenomenon is clearly observed in figure 17. Figure 17 shows the actual chord-line of cycloidal propeller blade and virtual chord-line due to virtual camber effect along different azimuth locations. It can be observed again at 0^0 azimuth, virtual camber is minimum producing almost negligible negative lift while at 180^0 azimuth it has huge negative virtual camber producing large negative lift.

Moreover, viewing from inertial reference frame, it can be observed from Fig. 17 that there is significant negative virtual camber when the blade operates in the upper half, which causes flow to separate very early. While, in the entire lower half, it creates a positive virtual camber, which delays flow separation and blade can attain much higher lift at these locations. Moreover, the virtual incidence decreases the effective angle of attack in the upper half and increases the angle of attack in the lower half. These are the reasons why the magnitude of maximum radial and tangential force coefficients in the downstream half (ψ = 180° – 360°) is significantly higher than that at upstream (ψ = 0° – 180°) (Figs. 13 and 14).

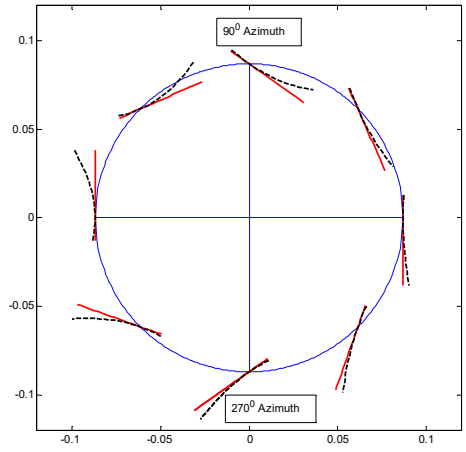

Fig. 17 Virtual chord-line due to virtual camber effect along azimuth.

4.2 Reason for Time-Averaged Side Forces

Another non-intuitive physical phenomenon observed during the operation of cycloidal propeller is asymmetric or non-negative net side force even with a symmetric prescribed pitch without any phase offset (T_y force shown in Fig. 2). From the kinematics shown in Fig. 2, intuitively, one may expect all the side forces due to drag and lift to cancel each other giving only a net vertical force; however, in reality, experiments have shown the presence of a dominating side force (Figs. 18 and 19). Figure 18 shows experimental comparison of time-averaged forces over a range of pitch amplitude. The results show existence of a non-zero time-averaged side force (T_y), even though significantly smaller in magnitude than the vertical force (T_z).

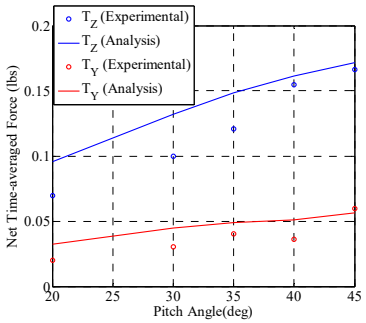

Fig. 18 Comparison time-averaged forces at different pitch amplitude.

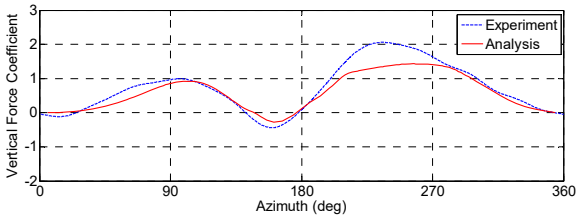

Fig. 19a Variation of instantaneous vertical forces along azimuth

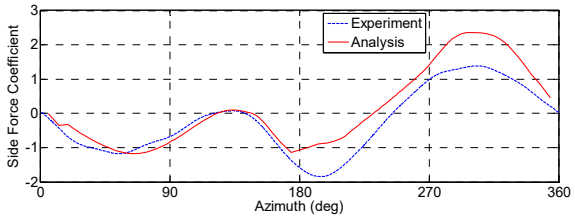

Fig. 19b Variation of instantaneous side forces along azimuth

Fig. 19 Comparison instantaneous vertical and side forces along azimuth (Pitch Amplitude: 45^0)

To investigate this phenomenon, instantaneous vertical and side forces are plotted and compared in Fig. 19. Figures 18 and 19, show extremely good correlation between results obtained from experiments and analysis. Instantaneous vertical and side forces are obtained using following expressions.

$$F_z = F_R \sin\psi - F_T \cos\psi \tag{33}$$

$$F_Y = -F_R \cos\psi - F_T \sin\psi \tag{34}$$

In the above equations, F_R is the radial force, F_T is tangential force, F_Z is vertical force and F_Y is side force at azimuth location, ψ. This phenomenon can be explained by dynamic virtual camber effect due to pitch rate and flow curvature. It can be observed from Eq. 34 that side force comes from two sources, radial and tangential forces. Radial force is mostly dominated by lift while tangential force is mostly dominated by drag. The relation between lift - drag and radial - tangential force are given by equations 35 and 36, where α is angle of attack.

$$F_R = L\cos\alpha + D\sin\alpha \tag{35}$$

$$F_T = L\sin\alpha - D\cos\alpha \tag{36}$$

Therefore, it should be possible to trace back the source of side force to lift and drag on the blade. The validated hydrodynamic model is used to investigate underlying reason behind non-zero time-averaged side force. In Fig. 20, side force due to lift and drag are plotted separately to distinguish their effects.

Figure 20a shows the contribution of instantaneous blade lift to side force. Note that, in this case, the X-axis is plotted differently to separate the left and right halves. It can be observed from Fig. 20a that if no virtual camber is considered (blue line), then side force due to lift is perfectly symmetric between left and right halves. Side force from left half of cycloidal propeller cycle ($\psi = 90^0$ – 270^0) cancels side force of right half ($\psi = 270^0$ – $450^0/90^0$), as seen from Fig. 2. The red line in figure 20a shows that once the virtual camber due to curvilinear flow geometry and pitch angle is incorporated, the side force is still symmetric between the left and right halves producing almost zero net side force. This is because virtual camber due to flow curvature introduces asymmetry between top half (upstream) and bottom half (downstream) of the cycle; the symmetry between right and left halves remains intact. But once the virtual camber due to pitch rate is introduced (black line in Fig. 20a), it causes significant asymmetry in side force between left and right halves causing non-zero net side force. This is because the propeller blade goes through pitch up motion during right half of cycle ($\psi = 270^0$ – $450^0/90^0$) while it goes through pitch down motion during left side of cycle ($\psi = 90^0$ – 270^0). As explained in the previous section, the pitch up motion causes positive virtual camber effect while pitch down motion creates negative camber effect. Due to this two opposite virtual camber effects in left and right halves, the side force gets unbalanced. This phenomenon becomes evident from Fig. 17 where it is observed that cycloidal propeller motion creates mild negative virtual camber on right side while it creates large negative camber on left side.

From Fig. 2, one may expect the drag at the top half (upstream) to be canceled by the drag at the bottom half (downstream). Figure 20b (contribution of instantaneous blade lift to side force) shows similar results when no virtual camber is included (blue line is antisymmetric between upper and lower halves). However, once the virtual camber due to flow curvature is included, the red line shows asymmetry in side force due to drag. It shows decrease in magnitude of side force in the upstream half while increase in magnitude of side force in the downstream half. This is because flow curvature creates almost equal negative camber everywhere. In the upstream half, geometric pitch is positive and thus, negative virtual camber decreases effective angle of attack which in turn causes decrease in magnitude of drag and corresponding side force. While in downstream half, the geometric pitch is negative and negative virtual camber creates larger negative effective angle of attack (observed from rotating blade frame) which causes larger magnitude of drag and corresponding side force. This phenomenon causes imbalance in side force due to drag.

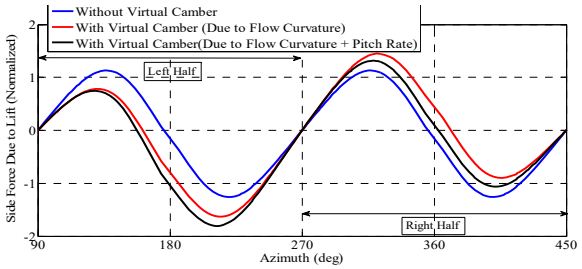

Fig. 20a Variation of side force due to lift along azimuth

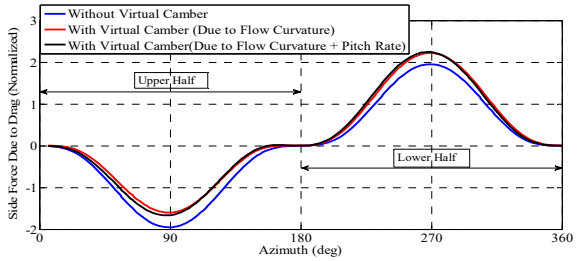

Fig. 20b Variation of side force due to drag along azimuth

Fig. 20 Effect of virtual camber on asymmetry of side force

(Pitch Amplitude: 45^0)

5 SUMMARY AND CONCLUSIONS

The primary goal of this study is to develop a lower order unsteady hydrodynamic model of cycloidal propeller that can predict instantaneous blade forces and propeller performance with sufficient accuracy that it could be utilized for design optimization of next generation of UUVs. Towards this, several underlying physical phenomena behind the operation of cycloidal propeller are thoroughly investigated. Dynamic virtual camber, effects of shed and near wakes, leading edge vortices and complex inflow characteristics are rigorously modeled. The developed hydrodynamic model is validated with measured time-history of fluid-dynamic forces obtained from in-house experimental data. The key conclusions from the study are given below:

1. Chord-wise variation of incident velocity angle on cycloidal propeller blade is manifested as virtual camber/incidence effect. Virtual camber and incidence depends on curvilinear flow geometry, pitch angle, pitch-rate and inflow distribution. Considering all these effects, a generalized methodology is developed to model virtual camber.

2. Curvilinear geometry causes a static negative virtual camber at all azimuth locations while pitch, pitch rate and inflow distribution causes cyclic variation of virtual camber with blade azimuthal location making it a dynamic virtual camber. A positive blade pitch-rate (nose-up pitch) creates positive virtual camber, while a negative pitch-rate (nose-down pitch) creates negative virtual camber.

3. Virtual camber caused by pitch rate creates asymmetry in side force due to blade lift between the right and left halves. However, the virtual camber resulting from flow curvature creates asymmetry in side force between upper and lower halves due to blade drag. These two types of asymmetries create net time averaged side force on a cycloidal propeller even with zero phase offset.

4. Due to curvilinear flow, the cycloidal propeller blade experiences reverse or negative virtual camber in the upper half (upstream half) of its circular trajectory along with decrease in effective angle of attack due to negative virtual incidence. However, the blade experiences positive virtual camber (observed from inertial frame) and increase in effective angle of attack (due to positive virtual incidence) in the entire lower half (downstream half). For this reason, blades produce larger hydrodynamic forces in the lower or downstream half as observed from both experiments and analysis. Moreover, unsteady phenomena such as dynamic stall keep the flow attached to cycloidal propeller blade up to very high pitch angles, which results in very high sectional force coefficients.

REFERENCES

Anderson, J. (1996). 'Vorticity control for efficient propulsion'. Ph.D. dissertation, Dept. Oceanographic Eng., Massachusetts Inst. Technol., Cambridge.

Bandyopadhyay, P. R. (2005). 'Trends in Biorobotic Autonomous Undersea Vehicles'. IEEE Journal of Oceanic Engineering, 30, 109–139.

Bartels, Jens-Erk, and Dirk Jürgens (2006). 'The Voith Schneider Propeller: Current applications and new developments'. Technical report, Voith Turbo Marine GmbH.

Benedict, M. (2010). 'Fundamental Understanding of the Cycloidal-Rotor Concept for Micro Air Vehicle Applications'. Ph.D. Thesis, Department of Aerospace Engineering, University of Maryland College Park.

Benedict, M., Gupta, R., and Chopra, I. (2013a). 'Design, Development and Flight Testing of a Twin-Rotor Cyclocopter Micro Air Vehicle'. Journal of the American Helicopter Society, Vol. 58, No. 4, pp. 1 – 10.

Benedict, M., Jarugumilli, T., and Chopra, I (2011a). 'Experimental Optimization of MAV-Scale Cycloidal Rotor Performance'. Journal of the American Helicopter Society, Vol. 56, No. 2, pp. 022005-1 - 022005-11.

Benedict, M., Jarugumilli, T., and Chopra, I. (2013b). 'Effect of Rotor Geometry and Blade Kinematics on Cycloidal Rotor Hover Performance'. Journal of Aircraft, Vol. 50, No. 5, pp. 1340 – 1352.

Benedict, M., Jarugumilli, T., Lakshminarayan, V. K., and Chopra, I. (2014a). 'Effect of Flow Curvature on the Forward Flight Performance of a MAV-Scale Cycloidal Rotor'. AIAA Journal (early edition).

Benedict, M., Mattaboni, M., Chopra, I., and Masarati, P. (2011b). 'Aeroelastic Analysis of a Micro-Air-Vehicle-Scale Cycloidal Rotor in Hover'. AIAA Journal, Vol. 49, No. 11, pp. 2430 – 2443.

Benedict, M., Mullins, J., Hrishikeshavan, V., and Chopra, I. (2013c). 'Development of an Optimized Quad Cycloidal-Rotor UAV Capable of Autonomous Stable Hover'. Proceedings of the American Helicopter Society International Specialists' Meeting on Unmanned Rotorcraft, Scottsdale, AZ.

Benedict, M., Ramasamy, M., and Chopra, I. (2010a). 'Improving the Aerodynamic Performance of Micro-Air-Vehicle-Scale Cycloidal Rotor: An Experimental Approach'. Journal of Aircraft, Vol. 47, No. 4, pp. 1117 – 1125.

Benedict, M., Ramasamy, M., Chopra, I., and Leishman, J. G. (2010b). 'Performance of a Cycloidal Rotor Concept for Micro Air Vehicle Applications'. Journal of the American Helicopter Society, Vol. 55, No. 2, pp. 022002-1 - 022002-14.

Benedict, M., Shrestha, E., Hrishikeshavan, V., and Chopra, I. (2014b), 'Development of a Micro Twin-Rotor Cyclocopter Capable of Autonomous Hover', Journal of Aircraft, Vol. 51, No. 2, pp. 672 – 676.

Blidberg, D. R. (2001). 'The development of autonomous underwater vehicles (AUV); a brief summary'. Proceedings of the IEEE Conference on Robotics and automation (ICRA 2001), Seoul, Republic of Korea, (IEEE, New York).

Bose, N., & Lai, P. S. K. (1989). 'Experimental performance of a trochoidal propeller with high-aspect-ratio blades'. Marine technology, 26(3) , pp. 192-201.

Budiyono, A. (2009). 'Advances in unmanned underwater vehicles technologies: modeling, control and guidance perspectives'. Indian J. Marine Sci., 38(3), 282–295.

Collar, P. G., Babb, R. J., Michel, J.-L., Brisset, L., and Kilpatrick, I. M. (1994). 'Systems research for unmanned autonomous underwater vehicles'. OCEANS '94, Oceans engineering for today's technology and tomorrow's preservation, Brest, France, pp. I/158–I/163 (IEEE, New York).

Dickerson, M. C., & Dobay, G. F. (1970). 'Experimental Performance of Some High-Pitch Cycloidal Propellers (No. SPD-399-01)'. DAVID W TAYLOR NAVAL SHIP RESEARCH AND DEVELOPMENT CENTER BETHESDA MD SHIP PERFORMANCE DEPT.

Esmailian, E., Ghassemi, H., & Heidari, S. A. (2014). 'Numerical Investigation of the Performance of Voith Schneider Propulsion'. American Journal of Marine Science, 2(3), 58-62.

Ficken, N. L., & Dickerson, M. C. (1969). 'Experimental Performance and Steering Characteristics of Cycloidal Propellers (No. NSRDC-2983)'. DAVID W TAYLOR NAVAL SHIP RESEARCH AND DEVELOPMENT CENTER BETHESDA MD.

Flores, M. (2003). 'Flapping motion of a three dimensional foil for propulsion and maneuvering of underwater vehicles'. M.S. thesis, Dept. Ocean Eng., Massachusetts Inst. Technology, Cambridge.

Griffiths, G., Jamieson, J., Mitchell, S., and Rutherford, K. (2004). 'Energy storage for long endurance AUVs'. Proceedings of the Conference on Advances in technologies for underwater vehicles, London, pp. 8–16 (Institute of Marine Engineering, Science and Technology, London).

Haberman, W. L., & Caster, E. B. (1962). 'Performance of vertical axis (cycloidal) propellers according to Isay's theory'. International Shipbuilding Progress, 9(90).

Haberman, W. L., & Harley, E. E. (1961). 'Performance of Vertical Axis (cycloidal) Propellers Calculated by Taniguchi's Method (No. DTMB-1564)'. DAVID TAYLOR MODEL BASIN WASHINGTON DC.

Haugsdal, O. (2000). 'Motion control of oscillating foils for steady propulsion and starting maneuvers'. M.S. thesis, Massachusetts Inst. Technol., Cambridge.

Hwang, I. S., Hwang, C. P., Min, S. Y., Jeong, I. O., Lee, C. H., Lee., Y. H., and Kim, S. J. (2006). 'Design and Testing of VTOL UAV Cyclocopter with 4 Rotors'. American Helicopter Society 62nd Annual Forum Proceedings, Phoenix, AZ.

Hwang, I. S., Hwang, C. S., and Kim, S. J. (2005). 'Structural Design of Cyclocopter Blade System'. Paper AIAA-2005-2020, 46th AIAA/ASME/ASCE/AHS/ASC Structures, Structural Dynamics and Materials Conference Proceedings, Austin, TX.

James, Edwin Charles. (1971). 'A small perturbation theory for cycloidal propellers', Doctoral Dissertation. California Institute of Technology.

Jarugumilli, T., Benedict, M., and Chopra, I. (2014). 'Wind Tunnel Studies on a Micro Air Vehicle-Scale Cycloidal Rotor'. Journal of the American Helicopter Society, Vol. 59, No. 2, pp. 1 – 10.

Jarugumilli, T., Benedict, M., Lind, A. H., and Chopra, I. (2013a). 'Performance and Flow Visualization Studies to Examine the Role of Pitching Kinematics on MAV-scale Cycloidal Rotor Performance in Forward Flight'. Proceedings of the American Helicopter Society International Specialists' Meeting on Unmanned Rotorcraft, Scottsdale, AZ.

Jarugumilli, T., Lind, A. H., Benedict, M., Lakshminarayan, V. K., Jones, A. R., and Chopra, I. (2013b). 'Experimental and Computational Flow Field Studies of a MAV-scale Cycloidal Rotor in Forward Flight'. Proceedings of the 69th Annual National Forum of the American Helicopter Society, Phoenix, AZ.

Jürgens, D., Palm, M., Singer, S., & Urban, K. (2007). 'Numerical optimization of the Voith-Schneider® Propeller'. ZAMM-Journal of Applied Mathematics and Mechanics/Zeitschrift für Angewandte Mathematik und Mechanik, 87(10), pp. 698-710.

Hrishikeshavan, V., Benedict, M., and Chopra, I. (2014). 'Identification of Flight Dynamics of a Cyclocopter Micro Air Vehicle in Hover'. Journal of Aircraft (early edition.

Iosilevskii, G., and Levy, Y. (2006). 'Experimental and Numerical Study of Cyclogiro Aerodynamics'. AIAA Journal, Vol. 44, No. 12, pp. 2866–2870.

Kato, N. (1998). 'Locomotion by mechanical pectoral fins'. Journal of marine science and technology, 3(3), pp. 113-121.

Kim, S. J., Hwang, I. S., Lee, H. Y., and Jung, J. S. (2004). 'Design and Development of Unmanned VTOL Cyclocopter'. Symposium on Aerospace Science and Technology Proceedings, NC.

Licht, S., Polidoro, V., Flores, M., Hover, F. S., and Triantafyllou, M. S. (2004). 'Design and projected performance of a flapping foil AUV'. IEEE Journal of Oceanic Engineering, 29(3), pp. 786-794.

Low, K. H. (2011). 'Current and future trends of biologically inspired underwater vehicles'. (pp. 1-8). IEEE. Defense Science Research Conference and Expo (DSR).

McNabb, M. (2001). 'Development of a Cycloidal Propulsion Computer Model and Comparison with Experiment'. M.S. Thesis, Department of Aerospace Engineering, Mississippi State Univ., Mississippi State, MS.

Navy, U. S. (2004). 'The navy unmanned undersea vehicle (UUV) master plan'. US Navy, 90.

Palmre, V., Hubbard, J. J., Fleming, M., Pugal, D., Kim, S., Kim, K. J., & Leang, K. K. (2013). 'An IPMC-enabled bio-inspired bending/twisting fin for underwater applications'. Smart Materials and Structures, 22(1), 014003.

Phillips, A. B., Blake, J. I., Smith, B., Boyd, S. W., & Griffiths, G. (2010). 'Nature in engineering for monitoring the oceans: towards a bio-inspired flexible autonomous underwater vehicle operating in an unsteady flow'. Proceedings of the Institution of Mechanical Engineers, Part M: Journal of Engineering for the Maritime Environment, 224(4), pp. 267-278.

Polhamus, E.C. (1966). 'A Concept Of The Vortex Lift Of Sharp-Edge Delta Wings Based On a Leading Edge Suction Analogy'. NASA Technical Note.

Polhamus, E.C. (1968). 'Application Of The Leading-Edge Suction Analogy Of Vortex Lift To The Drag Due To Lift Of Sharp-Edge Delta Wings'. NASA Technical Note.

Polidoro, V. (2003). 'Flapping foil propulsion for cruising and hovering autonomous underwater vehicles'. M.S. thesis, Dept. Ocean Eng., Massachusetts Inst. Technology, Cambridge.

Read, D. (1999). 'Oscillating foils for propulsion and maneuvering of ships and underwater vehicles'. M.S. thesis, Dept. Naval Architect. Marine Eng., Massachusetts Inst. Technol., Cambridge.

Roper, D. T., Sharma, S., Sutton, R., & Culverhouse, P. (2011). 'A review of developments towards biologically inspired propulsion systems for autonomous underwater vehicles'. Proceedings of the Institution of Mechanical Engineers, Part M: Journal of Engineering for the Maritime Environment, 225(2), pp. 77-96.

Shrestha, E., Benedict, M., Hrishikeshavan, V., and Chopra, I. (2012). 'Development of a 100 gram Micro Cyclocopter Capable of Autonomous Hover'. Proceedings of the 38th European Rotorcraft Forum, Amsterdam, Netherlands.

Shrestha, E., Hrishikeshavan, V., Benedict, M., Yeo, D., and Chopra, I. (2014). 'Development of Control Strategies and Flight Testing of a Twin-Cyclocopter in Forward Flight'. Proceedings of the 70th Annual National Forum of the American Helicopter Society, Montreal, Quebec, Canada.

Sparenberg, J. A., & De Graaf, R. (1969). 'On the optimum one-bladed cycloidal ship propeller'. Journal of Engineering Mathematics, 3(1), pp. 1-20.

Triantafyllou, M. S., Techet, A. H., & Hover, F. S. (2004). 'Review of experimental work in biomimetic foils'. Oceanic Engineering, IEEE Journal of, 29(3), pp. 585-594.

Triantafyllou, M. S., Triantafyllou, G. S., & Yue, D. K. P. (2000). 'Hydrodynamics of fishlike swimming'. Annual review of fluid mechanics, 32(1), pp. 33-53.

Walther, C.M., Coleman, D., Benedict, M. & Lakshminarayan, V., (2017). 'Experimental and Computational Studies to Understand Unsteady Aerodynamics of Cycloidal Rotors in Hover at Ultalow Reynolds Number'. AHS International's 73rd Annual Forum.

Wheatley, J. (1933). 'Simplified Aerodynamic Analysis of the Cyclogiro Rotating-Wing System'. National Advisory Committee for Aeronautics, TR 467.

Wheatley, J. B., & Windler, R. (1935). 'Wind-Tunnel Tests of a Cyclogiro Rotor'. NACA Technical Note No. 528.

Zachary, H., A., Benedict, M., Hrishikeshavan, V., and Chopra, I. (2013). 'Design, Development, and Flight Test of a Small-Scale Cyclogyro UAV Utilizing a Novel Cam-Based Passive Blade Pitching Mechanism'. International Journal of Micro Air Vehicles, Vol. 5, No. 2, pp. 145 – 162.

Zhou, C., & Low, K. H. (2012). 'Design and locomotion control of a biomimetic underwater vehicle with fin propulsion'. IEEE/ASME Transactions on Mechatronics, 17(1), pp. 25-35.

Zhu, D. M. (1981). 'A Computational Method for Cycloidal Propellers'. International Shipbuilding Progress, 28, pp. 102-111.